Northumbria Research Link

Metal Contact and Carrier Transport in Single Crystalline $CH_3NH_3PbBr_3$ Perovskite

Chun-Ho Lin, Ting-You Li, Bin Cheng, Changxu Liu, Chih-Wen Yang, Jr-Jian Ke, Tzu-Chiao Wei, Lain-Jong Li, Andrea Fratalocchi, Jr-Hau He

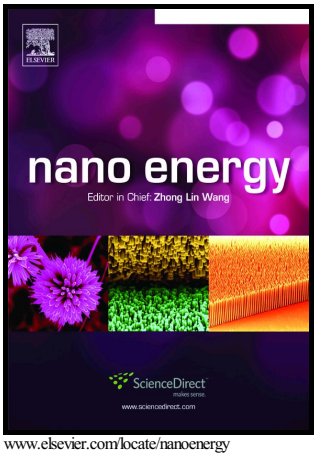

www.elsevier.com/locate/nanoenergy

PII: S2211-2855(18)30693-1
DOI: https://doi.org/10.1016/j.nanoen.2018.09.049
Reference: NANOEN3054

To appear in: *Nano Energy*

Received date: 7 July 2018
Revised date: 18 September 2018
Accepted date: 19 September 2018

Cite this article as: Chun-Ho Lin, Ting-You Li, Bin Cheng, Changxu Liu, Chih-Wen Yang, Jr-Jian Ke, Tzu-Chiao Wei, Lain-Jong Li, Andrea Fratalocchi and Jr-Hau He, Metal Contact and Carrier Transport in Single Crystalline $CH_3NH_3PbBr_3$ Perovskite, *Nano Energy,* https://doi.org/10.1016/j.nanoen.2018.09.049

Metal Contact and Carrier Transport in Single Crystalline $CH_3NH_3PbBr_3$ Perovskite

Chun-Ho Lin[a], Ting-You Li[a], Bin Cheng[a], Changxu Liu[a, b], Chih-Wen Yang[c], Jr-Jian Ke[a], Tzu-Chiao Wei[a], Lain-Jong Li[c], Andrea Fratalocchi[a], and Jr-Hau He[a*]

[a]Computer, Electrical, and Mathematical Sciences and Engineering (CEMSE) Division, King Abdullah University of Science & Technology (KAUST), Thuwal 23955-6900, Saudi Arabia.

[b]School of Physics & Astronomy, University of Birmingham, Birmingham B15 2TT, United Kingdom.

[c]Physical Science and Engineering (PSE) Division, King Abdullah University of Science & Technology (KAUST), Thuwal 23955-6900, Saudi Arabia.

[*]Corresponding author. *Email address:* jrhau.he@kaust.edu.sa (J. H. He).

Abstract:

Organic-inorganic perovskites have arrived at the forefront of solar technology due to their impressive carrier lifetimes and superior optoelectronic properties. By having the cm-sized perovskite single crystal and employing device patterning techniques, and the transfer length method (TLM), we are able to get the insight into the metal contact and carrier transport behaviors, which is necessary for maximizing device performance and efficiency. In addition to the metal work function, we found that the image force and interface charge pinning effects also affect the metal contact, and the studied single crystal $CH_3NH_3PbBr_3$ features Schottky barriers of 0.17 eV, 0.38 eV, and 0.47 eV for Au, Pt, and Ti electrodes, respectively. Furthermore, the surface charges lead to the thermally activated transport from 207 K to 300 K near the perovskite surface. In contrast, from 120 K to 207 K, the material exhibited three-dimensional (3D) variable range hopping (VRH) carrier transport behavior. Understanding these fundamental contact and transport properties of perovskite will enable future electronic and optoelectronic applications.

Graphical abstract

Keywords:

Perovskite; $CH_3NH_3PbBr_3$; Metal contact; Schottky barrier; Carrier transport

1. Introduction

Organic-inorganic hybrid perovskite-based ($MAPbX_3$, MA = $CH_3NH_3^+$; X = Cl^-, Br^- or I^-) photovoltaics are rapidly challenging established solar technologies. In just a few years, researchers have found ways to increase the power efficiency of planar heterojunction perovskite solar cells to over 20%, making it the fastest-advancing photovoltaic technology to date [1-5]. Moreover, these solar cells have low production costs, which could make perovskite modules competitive in the marketplace [6]. With superior optoelectronic properties, perovskites also demonstrate strong prospects in other applications, such as light emission and lasing [7-9].

However, due to grain boundary defects, the electron-hole diffusion lengths in amorphous and polycrystalline perovskite thin films are small, limiting the efficiency of photo-generated charge collection [10]. Furthermore, several key obstacles currently prevent commercialization of perovskite electronics and optoelectronic technologies. For example, the performance of perovskite solar cells tends to vary, with an average efficiency that is typically 4–10% lower than the highest efficiency reported [11]. Additionally, the appearance of hysteresis effects in *I-V*

measurements suggests perovskites suffer from reproducibility and stability issues that must be overcome to move the technology forward [12,13]. However, the use and study of polycrystalline perovskites inhibit the full understanding on these materials as the low crystal quality obscures intrinsic electrical and optoelectronic properties.

In response, researchers have devoted considerable efforts to synthesizing mm-scale single crystal perovskites that are free of grain boundary defects [14-17] to enable a variety of high-performance applications, including photodetection, gas sensing, and photovoltaics [18-20]. These kinds of high quality perovskites mitigate hysteresis effects owing to the lower density of defects, which reduces charge trapping during device operation and leads to higher carrier mobilities and diffusion lengths [16]. In fact, ultra-long electron-hole diffusion lengths >175 μm have been reported in single crystal $CH_3NH_3PbI_3$, which is significantly larger than the diffusion lengths in amorphous or polycrystalline thin films (several hundred nanometers) [15]. Single crystal perovskites also provide an ideal platform to gain insights into the materials' fundamental properties, which would enable us to explore the limits of device performance.

In addition to using single crystal perovskites, the key to achieving better device performance is to control charge carrier flow, including by means of charge injection and carrier transport. Beginning with charge injection, the electrical contact between the electrode and the

active material is known to play a decisive role in determining device performance [21]. Perovskite-based solar cells commonly use organic hole transport layers, such as 2,2',7,7'-tetrakis(N,N'-di-p-methoxyphenylamine)-9,9'-spirobifluorene (spiro-OMeTAD) and poly (3-hexylthiophene) (P3HT). However, these materials are unstable in moisture [22,23], which means additional device protection or sealing is necessary for practical use. Since no encapsulation system is perfect, the degradation of such compounds over time may contribute to the reproducibility issues associated with perovskites. Furthermore, the price of spiro-OMeTAD and P3HT is almost ten times higher than that of Au [24,25].

In contrast, metals typically have high resistance when exposed to humidity, and therefore single crystal perovskites contacted to metal electrodes are more stable in air, preventing degradation of device performance and retaining the material's electrical properties for as long as 25 days at 50% average humidity (Fig. S1). Considering the excellent humidity resistance, cost-effectiveness, and precisely controlled electrical/optoelectronic properties, the development of metal contacts for single crystal perovskites is crucial. The investigation of the metal contact of perovskite can help us to achieve efficient carrier injection from electrode to perovskite, in which the contact resistance is minimized in order to prevent significant energy loss or carrier scattering at the interface of the metal/semiconductor (MS) junction.

Understanding the carrier transport mechanism in perovskites is also important for learning how to increase device efficiency. Up to date, due to challenges in large crystal growth method, and robust perovskite device patterning technique enabling the measurement of transport properties, only indirect experimental characterization techniques have been reported in recent years, such as mobility measurements, terahertz, and time-resolved photoluminescence, to observe the scattering and carrier recombination in the perovskite crystal [26-29]. Moreover, due to the existence of trap states, mobile ions, ferroelectricity, and interface charge in perovskite, the carrier transport is complicated and highly depend on the crystal growth method [30]. Briefly speaking, the research on the carrier transport in perovskite is still in infancy stage. More direct investigation of temperature dependent conductivity of perovskites can help us to gain insights into the transport mechanism.

In this study, we have investigated the metal contact and carrier transport mechanisms of single crystal $CH_3NH_3PbBr_3$, which was grown using the anti-solvent vapor-assisted crystallization method (AVC) [16]. We deposited a variety of metals (Au, Pt, and Ti) as the electrodes on the surface of the perovskite to study the Schottky contact at the MS junction. The ideal Schottky barrier height for $CH_3NH_3PbBr_3$ contacted with Au, Pt, and Ti should be 0.6 eV, 0.15 eV, and 1.27 eV, according to the electron affinity model. However, our results show that the experimental Schottky barrier height for Au, Pt, and Ti contacts with this perovskite are 0.17

eV, 0.38 eV, and 0.47 eV, which we attribute to the influence of image forces and interface pinning effects. The carrier transport mechanism was investigated on lithography patterned perovskite device using the TLM, which can eliminate the influence of contact resistance and helpful to measure the conductivity of the perovskite itself [31-34]. By studying the current flows near the surface of $CH_3NH_3PbBr_3$ crystal, our results suggest that the surface charges would induce the thermally activated transport in the temperatures ranging from 207 K to 300 K with an activation energy around 0.2 eV. On the other hand, a 3D VRH conduction mechanism dominates current transport from 120 K to 207 K. We also confirmed the VRH carrier behavior with various Mott parameters. This study of the metal contact and carrier transport properties in single crystal $CH_3NH_3PbBr_3$ provides fundamental knowledge that can be used to optimize future perovskite-based device performance.

2. Materials and experiments

2.1 Materials

The following reagents and materials were purchased from Sigma-Aldrich and used without further purification: hydrobromic acid (48 wt% in H_2O, ≥99.99%), lead(II) bromide (≥98%), methylamine (40 wt% in H_2O), ethanol (≥99.8%), diethyl ether (anhydrous, ≥99.0%),

N,N-dimethylformamide (DMF; anhydrous, 99.8%), dichloromethane (DCM; anhydrous, ≥99.8%), and 4a molecular sieve. We also purchased hexane (HPLC) from Fisher Chemical.

2.2 Single crystal $CH_3NH_3PbBr_3$ synthesis

First, an equimolar amount of hydrobromic acid and methylamine were mixed together and stirred for 2 h at 10 °C to form the precursor, methylammonium bromide (CH_3NH_3Br), which we recrystallized in ethanol. Next, we dissolved an equimolar amount of $PbBr_2$ and the CH_3NH_3Br crystals in DMF. $CH_3NH_3PbBr_3$ single crystals were then grown by the AVC method [16], in which the anti-solvent DCM vapor diffused into the DMF. Note that the perovskite can only crystalize when the diffusion rate of the DCM vapor is slow. To achieve the slow diffusion rate, we covered the glass sample vial with parafilm featuring a small pinhole. The perovskite crystal sizes were highly dependent on the surrounding temperature, as shown in Fig. S2. We removed the crystals from the DMF and cleaned them with lens paper soaked in anhydrous hexane (hexane and 4a molecular sieve, 1:1 volume).

2.3 Perovskite crystal grinding and polishing

We coated diamond paste (mesh 8000, Best Diamond Industrial Co., Ltd.) on an electric grinder (Taiwan Po workers PT-5721F) and ground the perovskite crystals for 10 mins (5000 rpm). Then, the crystal surfaces were polished with lens papers and different diamond grinding

pastes in sequence (mesh 8000, mesh 28000, mesh 60000, mesh 200000). We ran each paste-polishing step 200 times. After polishing, we cleaned the crystals with lens paper and anhydrous hexane.

2.4 Experiments

To investigate the Raman and photoluminescence (PL) properties of single crystal $CH_3NH_3PbBr_3$, we employed a confocal Raman/fluorescence microscope system (NTEGRA Spectra, NT-MDT) using a laser with an excitation wavelength of 473 nm and a spot size of ~0.5 μm in diameter. The micro-Raman spectra were measured using a backscattering geometry and the incident laser light propagated parallel to the z-axis of the $CH_3NH_3PbBr_3$ single crystals at different polarization angles. The UV-vis absorption spectrum of the perovskite was obtained using a Shimadzu UV 3600 spectrophotometer. For single crystal X-ray diffraction (XRD) measurement, a small fraction of the crystal (~0.1 × 0.1 × 0.08 mm^3) was cleaved from the as-grown $CH_3NH_3PbBr_3$, and structural details were confirmed using a Bruker KAPPA APEX DUO Diffractometer featuring IμS Cu radiation at 296 K (λ = 0.71073 Å), an APEX II 4K CCD detector, and a microfocus X-ray source. Phase purity was investigated with powder XRD using a Bruker D8 Advance diffractometer (Bragg–Brentano geometry) equipped with a Cu Ka X-ray tube. Thermogravimetric analysis (TGA) of both single crystalline and polycrystalline $CH_3NH_3PbBr_3$ was performed at a heating rate of 2 ºC/min, from 25 ºC up to 600 ºC under

nitrogen atmosphere using a NETZSCH TGA/STA-QMS 403 C. For scanning kelvin probe microscopy (SKPM) measurement, the surface morphology and surface potential of the sample was examined with a multifunction atomic force microscope (Cypher ES - Asylum Research Oxford Instruments). Asylum research Ti/Pt-coated silicon cantilevers were used for the experiment. The tip curvature radius was ~28 nm and the resonance frequency was ~70 kHz. For photoelectron spectroscopy in air (PESA) measurement, the ionization potential of the single crystal $CH_3NH_3PbBr_3$ was investigated with a photoelectron spectrometer (Riken Keiki AC-2) in air with a UV power setting of 35 nW. For *I–V* characterization, a Keithley 4200-SCS semiconductor characterization system was used to measure the *I–V* curves of the single crystal $CH_3NH_3PbBr_3$ at various temperature conditions. The temperature control was performed with a Lakeshore 336 Temperature Controller in combination with an EverBeing Cryogenic Probe Station CG-196-200.

3. Results and Discussion

We grew high-quality, cm-sized single crystal $CH_3NH_3PbBr_3$ using the AVC method (Fig. 1a). This particular perovskite was chosen for study because it is stable in air and has a planar surface. In contrast, AVC-synthesized $CH_3NH_3PbI_3$ is relatively unstable [22] and $CH_3NH_3PbCl_3$ is visible-blind [35] because of its wide bandgap (2.88 eV), which precludes its use in solar

applications. We characterized the $CH_3NH_3PbBr_3$ with a variety of techniques, beginning with XRD of powders ground from the sample's large crystals. The XRD spectrum revealed sharp, strong peaks that agreed with the calculated results, indicating the high purity of the $CH_3NH_3PbBr_3$ crystal (Fig. 1b). Single crystal XRD analysis (Tables S1 and S2) indicated the material featured a cubic lattice structure, as shown in Fig. 1c. We also measured the Raman spectra of the $CH_3NH_3PbBr_3$ crystal rotated around its perpendicular axis to control the relative incident polarization angle of the 473 nm laser excitation. The periodic Raman intensity of the most intense peak (332 cm^{-1}) as a function of the rotation angle indicates that the $CH_3NH_3PbBr_3$ is single crystalline according to Raman selection rules (Fig. 1d) [36,37]. Additionally, the optical absorption spectra revealed a sharp band edge cut-off that corresponded to the perovskite's bandgap of 2.3 eV (E_g), which we obtained from the PL spectrum (Fig. 1e).

Another important physical feature of perovskites is their thermal stability [38]. According to TGA measurement, the crystal starts to crack at 320 ^oC (Fig. 1f), demonstrating the robustness of the single crystal $CH_3NH_3PbBr_3$ material compared to the polycrystalline version, which begins to crack around 210 ^oC (Fig. S3). We also conducted Hall effect measurements at room temperature and estimated the carrier concentration of single crystal $CH_3NH_3PbBr_3$ to be in the range of $5x10^{10}$ cm^{-3} to $3x10^{11}$ cm^{-3}, while the mobility was between 30 cm^2 V^{-1} s^{-1} and 55 cm^2 V^{-1} s^{-1}. Moreover, the single crystal $CH_3NH_3PbBr_3$ displayed p-type behavior in the Hall

measurements, indicating that hole transport dominates the perovskite's electrical properties [39,40].

Using a shadow mask, we fabricated different metal-semiconductor-metal (MSM) structures on the surface of the $CH_3NH_3PbBr_3$ crystals by sputtering 100 nm thick Pt, Au, and Ti electrodes with a spacing of 100 μm, which feature a wide range of metal work functions (Pt = 5.65 eV, Au = 5.1 eV, Ti = 4.33 eV) [41]. In this study, we treated the perovskite as a semiconductor, which is assumed to form a Schottky barrier at the MS interface. The equivalent circuit consists of a resistor and two back-to-back Schottky diodes (Fig. 2a) [42]. Then we surveyed the *I-V* characteristics of the samples made with Pt, Au, and Ti electrodes using a Keithley 4200 semiconductor characterization system (Fig. 2b). For all three metals, the *I-V* curves show exponential increase in current with voltage, demonstrating the perovskite displays Schottky behavior rather than Ohmic [43], which is in agreement with our previous assumption that the single crystal $CH_3NH_3PbBr_3$ can form a Schottky barrier at the MS interface. Furthermore, the normalized *I-V* curves demonstrate that the Au contact has the smallest turn-on voltage, implying the Schottky barrier height at the interface of the Au/perovskite junction is lower than that for the Pt and Ti/perovskite junctions. Here, the AVC-synthesized perovskite single crystal shows insignificant hysteresis effect in *I-V* measurements under different scan rates as shown in Fig. S4, which helps us to study the Schottky barrier height more precisely.

We next explored charge injection through the Schottky contacts using temperature-dependent *I-V* measurements. The two-probe *I-V* measurements, performed on the perovskite with Au electrodes at temperatures ranging from 200 K to 275 K, show that resistivity decreased with temperature, indicating the insulating behavior of the $CH_3NH_3PbBr_3$ (Fig. 2c). We can explain the perovskite's insulating behavior by the fact that its Fermi energy level lies in the region of the localized states that are below the lowest level of its conduction band, leading to a shortage of free carriers. When temperature increases, more thermally excited carriers jump to the conduction band, resulting in decreasing resistivity.

The total resistance (R_t) of the MSM system can be treated as a series of the forward-biased junction resistance (R_f), the resistance of the perovskite (R_p), and the reverse-biased junction resistance (R_r). At low bias (we applied a bias lower than 1 V for measuring the metal/perovskite Schottky contact), the charges will meet a much greater resistance on the reverse-biased side, and therefore the relatively small R_f and R_p values can be neglected [44,45]. As a result, the reverse-biased Schottky junction dominates the total voltage drop, which we can analyze using different charge injection models. Single crystal perovskites with ultra-long carrier diffusion lengths are more appropriately described by thermionic emission theory, which assumes that no collision occurs between carriers in the depletion region [46]. According to thermionic emission, phonon thermal energy excites the charge carriers and emits them over the barrier, resulting in a

current flow that depends exponentially on temperature. The saturation current density in the reverse-biased junction can be described as [21,47]

$$J = A^{**}T^{2}\,\mathrm{exp}\left(\frac{-q\Phi_{BE}}{K_{B}T}\right), \quad (1)$$

in which A^{**} is the equivalent Richardson constant, q is the electron charge, Φ_{BE} is the effective Schottky barrier height, and K_B is the Boltzmann constant. Based on Equation 1, the bias-dependent Φ_{BE} can be determined from the slope of ln (J/T^2) versus 1/T, which is shown in Fig. 2d-f for the Au, Pt, and Ti contacts, respectively. From these results, we found that Φ_{BE} decreased as the bias increased. For example, for the Au contact, the Φ_{BE} was 153 meV at 0.5 V bias and 144 meV at 1 V bias. The lowering of the effective barrier height with increasing bias voltage suggests that the image force plays an important role in the Schottky junction. Due to image force lowering of the Schottky barrier [48], the effective barrier height becomes lower than the ideal value. When the carriers approach the junction interface from the metal side, the corresponding image charges are built up at the perovskite surface due to the change of electric field. Then, the attracting image force between the carrier and its image charge is generated, which reduces the Schottky barrier height at the junction interface. In addition, the potential of the image charges grows simultaneously when the applied voltage increases, leading to a

voltage-dependent lowering of the barrier. This Schottky barrier lowering is described by two equations in image force theory, including [21]

$$\Phi_{B\,E} = \Phi_{B} - \sqrt{\frac{qE}{4\pi\varepsilon_p}} \tag{2}$$

and

$$E = \sqrt{\frac{2qN_D}{\varepsilon_p}\left(\mathrm{V} + \Phi_{bi} - \frac{K_B T}{q}\right)}, \tag{3}$$

in which Φ_{B0} is the barrier height in the absence of the image force, E is the maximum electric field at the junction, ε_p is the dielectric constant, N_D is the doping concentration of the single crystal perovskite, and Φ_{bi} is the built-in potential. To simplify the equation, the thermal energy (K_BT) can be neglected compared to Φ_{bi} and V. By combining $\Phi_{bi} = \Phi_{B0} - K_B T \ln\left(\frac{N_C}{N_D}\right) \approx \Phi_{B0}$ with Equation 2 and 3, where N_C is the effective conduction band density of states, we can obtain Φ_{BE} as

$$\Phi_{BE} \cong \Phi_{B0} - \sqrt{\frac{q}{4\pi\varepsilon_p}\sqrt{\frac{2qN_D}{\varepsilon_p}\left(\mathrm{V} + \Phi_{B0}\right)}}\,. \tag{4}$$

According to Equation 4, the Φ_{B0} and Φ_{E0} can be determined by least squares fitting of Φ_{BE} versus $(\mathrm{V}+\Phi_{B0})^{1/4}$, in which Φ_{E0} is the effective barrier height when the applied voltage is zero, as

shown in Fig. 2g. As a result, we calculated Φ_{E0} values of 0.17 eV, 0.38 eV, and 0.47 eV for the Au, Pt, and Ti contacts, respectively, and the corresponding Φ_{B0} values were 0.22 eV, 0.55 eV, and 0.74 eV.

At the MS junction, the Schottky barrier is the comprehensive result of the metal work function, image force, and interface states. The ideal Schottky barrier height (Φ_{Bi}) between a metal and p-type semiconductor can be predicted by the electron affinity model: [43]

$$\Phi_{Bi} = IP_p - \Phi_m, \quad (5)$$

in which IP_p is the ionization potential of a p-type semiconductor and Φ_m is the work function of the contact metal. Fig. 3a,b illustrate the band diagrams of Φ_{Bi} and Φ_{B0} for the Au contact. We determined the work function (Φ) and electron affinity (χ) of single crystal $CH_3NH_3PbBr_3$ from SKPM and PESA measurements, as shown in Fig. S5 and S6. According to Equation 5, the Φ_{Bi} between $CH_3NH_3PbBr_3$ and the Au electrodes is 0.6 eV, whereas the barrier height in the absence of the image force from Fig. 2f was 0.22 eV. The difference in these values indicates that the surface pinning effect occurs at the Au/perovskite junction interface.

For a defect-free interface, the Schottky barrier is determined by the charge neutrality level of metal-induced gap states. However, in a real case, the defects at the perovskite surface tend to capture electrons and form the interface dipoles, which give rise to charge rearrangement upon

the formation of the MS interface. Although all electronic measurements were taken under vacuum, we did fabricate the device in air, thus exposing the materials to moisture. It has been reported that water molecules in air will adsorb on the surface of single crystal $CH_3NH_3PbBr_3$, leading to the formation of a polycrystalline-like structure that forms surface states [49] (unlike polycrystalline $CH_3NH_3PbBr_3$, in which water molecules can damage the whole crystal along the grain boundary). Additionally, although we used low-voltage sputtering for contact electrode deposition, the sputtering damage may still exist, leading to the surface states at junction interface. As a result, the Fermi level near the interface is pinned by these surface states, which lowers the Schottky barrier height, as shown in Fig. 3b. We observed similar behavior with Pt and Ti electrodes on the perovskite, in which the surface defect trapped electrons form interface dipoles, resulting in a dipole-induced shift in the Schottky barrier height, as shown in Fig. S7 (Φ_{Bi} for $CH_3NH_3PbBr_3$ contacted with Pt and Ti electrodes are 0.15 eV and 1.27 eV, whereas Φ_{B0} are 0.55 eV and 0.74 eV, respectively). One can see that the pinning effect at perovskite/Ti interface is stronger than the other two samples, which implies the Ti electrode is more sensitive to the oxygen than Au and Pt electrodes.

Due to the fast development of perovskite solar cells, today, most of perovskite contact studies focus on the charge transport materials to improve the current injection and extraction in solar cells. Several nonmetal materials have shown the potential to achieve efficient

charge-collecting contact with perovskite, including electron transport materials (PCBM, PEHT, ICBA, TiO_2, ZnO, SnO_2, WO_x, *etc.*) and hole transport materials (spiro-OMeTAD, P3HT, PEDOT:PSS, PTAA, NiO, Cu2O, CuI, CuSCN, *etc.*) [50,51]. Besides the proper use of materials, gate-induced band alignment is also proposed recently to achieve the perovskite Ohmic contact [52]. Our study focuses on the perovskite metal Schottky contact, which is very important for the applications other than solar cells. This fundamental understanding of Schottky barrier height can help us further develop the perovskite electronics, including diodes, transistors and other electronic components, since these devices involve the proper design of the barrier height of their active materials. As a proof-of-concept demonstration, we have fabricated a Schottky diode using Au and Ti contacts where the junction is formed between Ti and perovskite, creating a Schottky barrier. Fig. 4 shows the *I-V* characteristics of the perovskite Schottky diode. Without extensive optimization of Schottky diode parameters, the obtained ON/OFF current ratio can be greater than 10 when the voltage changes from +5 to -5 V. The turn-on voltage of Schottky diode is around 0.2 V, demonstrating close agreement with the Schottky barrier height of Au/perovskite contact.

Another important concern for efficient current injection is the contact resistance between the active material and the metal electrode. To estimate the contact resistance, we performed the TLM measurements on the perovskite [31-34]. 100-nm-thick Au, which is expected to have

smaller contact resistance due to the fact that it has the lowest Schottky barrier in this case, was deposited onto the perovskite surface in the TLM structure [31,53] using e-beam lithography method. Note that depositing micron-scale electrodes or smaller patterns on the perovskite surface is difficult due to the high surface roughness of the AVC-synthesized crystal. Therefore, we polished the perovskite (see Materials and experiments) to smoothen its surface, which enables us to successfully deposit the metal electrodes on the sample by e-beam lithography. A scanning electron microscopy (SEM) image of the patterned electrodes on the perovskite is shown in Fig. 5a. In the MSM structure of the TLM configuration, the total resistance (R_T) is obtained by a two-terminal measurement that can be described by [43,54]

$$R_T = 2R_C + R_i \tag{6}$$

in which R_C is the contact resistance and R_i is the perovskite bulk resistance. Here, the two contact resistances of the MSM structure are assumed to be the same when the applied voltage is large. Because contact resistance is highly dependent on the contact area, we defined the specific contact resistance (ρ_c) to be $\rho_c = R_C \times A_C$, in which A_C is the active contact area [55]. Substituting ρ_c and $R_i = \rho \times \frac{L}{A}$ into Equation 6, where ρ is the resistivity of the perovskite, L is the distance between the two electrodes, and A is the cross-sectional area of the current flow, the total resistance becomes

$$R_T = \frac{2\rho_c}{A_C} + \rho\frac{L}{A}. \quad (7)$$

The TLM suggests a way to measure the contact resistance by constructing a series of resistors with several different lengths and measuring the R_T of each while keeping all other conditions the same. According to Equation 7, ρ can be evaluated from the slope of R_T against a fitting line of L, and ρ_c can be obtained when L is zero. To calculate ρ and ρ_c, we performed a simulation of current flow distribution in the device to confirm A_C and A, as shown in Fig. 5b. The simulated result shows that only 1.44 x 10^{-7} cm^2 of the Au electrodes (18% of the electrode areas) were effectively in contact with the perovskite single crystal, and the A was 2.26 x 10^{-6} cm^2. Details of the simulation and TLM can be found in Fig. S8 and S9 of the Supporting material.

Fig. 5c shows that ρ_c decreases with bias, echoing the results of Equation 4, which demonstrates that the image force-induced barrier height lowered more as the applied voltage was increased. In contrast, the resistivity of the perovskite remained constant as the bias changed from 2 V to 5V (Fig. 5d). Temperature-dependence is a key way to verify the electrical characteristics of a material. Therefore we also measured the ρ_c of the sample as the temperature ranged from 100 K to 300 K via the TLM (Fig. 5e). The strong temperature-dependence of ρ_c signifies that more charge carriers have enough thermal energy to overcome the Au/perovskite Schottky barrier

height at higher temperatures. The temperature-dependent resistivity shown in Fig. 5f again confirms the insulating behavior of the single crystal $CH_3NH_3PbBr_3$. As temperature increases, the charge carriers in the confined region gain sufficient energy to escape to the conduction band, enhancing the free carrier concentration and resulting in a reduction of the bulk resistivity.

To better understand the carrier transport and hopping in bulk $CH_3NH_3PbBr_3$, we further investigated the temperature dependence of the conductivity (σ, the inverse of resistivity). Fig. 6a shows the Arrhenius plots of the conductivity at temperatures ranging from 207 K to 300 K, indicating that thermally activated transport dominates this temperature region [56], a process that is described by Equation 8:

$$\sigma = C \exp\left(\frac{-E_a}{K_B T}\right), \tag{8}$$

in which C is a constant and E_a is the activation energy. To further study the transport mechanism at temperatures lower than 207 K (where the data deviates from the Arrhenius plot), we fit the results with multiple carrier transport models and find the best match with 3D VRH transport (Fig. 6b), which suggests that

$$\sigma = \sigma_0 \exp\left[-\left(\frac{T_0}{T}\right)\right]^{1/4}, \tag{9}$$

in which σ_0 is a constant at certain temperatures, and T_0 is the degree of disorder (T_0 = 288 x 10^4 K in this case) [57]. A schematic of thermally activated transport and the 3D VRH mechanism is shown in Fig. 6c.

Because the mobile ionic carriers exist (including ions MA^+, Pb^{2+}, X^- and vacancies V_{MA}, V_{Pb}, V_X), ionic carriers and charge carriers are believed to form the joint transport in hybrid perovskite [52,58,59]. The ionic carriers are expected to follow thermally activated transport while charge transport is determined by the charge-carrier−phonon scattering [26,27,60,61]. Thus, the growth and quality of crystal can significantly interfere with the transport. In the high-temperature region from 207 K to 300 K, our experiment result shows the thermally activated conduction dominates in perovskite. However, the ionic transport cannot dominate the transport in this study, since the high quality of perovskite was confirmed by single crystal XRD and angular dependent Raman, and the hysteresis effect is not obvious during measurements.

Since the measured current flows along the surface of perovskite as shown in Fig. S8b, the carrier scattering should be affected by the surface charges, which we have mentioned previously in the metal contact pinning effect. The surface charges can result in the carrier−defect scattering and thus the current transport turns into thermally activated transport in the perovskite surface region. Furthermore, from the linear part of the curve in Fig. 6a, we determined that E_a of the

thermal activation was approximately 0.2 eV. This small E_a value confirms that the thermally activated transport is caused by the defect level.

Conversely, in the low-temperature region below 207 K, the effect of the surface charge induced thermal activation decays and the VRH transport dominates the carrier conduction. Owing to the eliminated contact barrier by the TLM and the high quality of $CH_3NH_3PbBr_3$ single crystal, we can evaluate the VRH by 3D mode transport and verify the related Mott parameters. Mott's 3D VRH transport model [57] suggests that electric transport takes place due to hopping of the carriers between the localized states. Note that charge carrier hopping is not restricted to the neighboring states as long as the thermal energy matches the energy difference between the hopping states by a comparable order of a few K_BT. Furthermore, the temperature dependent PL measurement (Fig. S10) shows a peak-wavelength shift around 120 K, which can be attributed to the tetragonal-to-orthorhombic phase transition of single crystal $CH_3NH_3PbBr_3$ [62,63]. In the tetragonal phase and the temperature region from 120 K to 207 K, the charge carriers in perovskite follow 3D mode VRH transport. However, for the transport in orthorhombic phase below 120 K, although it is reported that the VRH occurs in the orthorhombic phase perovskite [52], we cannot conclude a specific mode of VRH here due to insufficient data below 100 K.

To investigate the individual 3D VRH Mott parameters of the single crystal $CH_3NH_3PbBr_3$ (such as hopping distance and energy), σ_0 and T_0 in Equation 9 can be expressed as

$$\sigma_0 = 3e^2\gamma\left[\frac{N(E_F)}{8\pi\alpha K_B T}\right]^{1/2} \quad (10)$$

and

$$T_0^{1/4} = \frac{\lambda\alpha^3}{K_B N(E_F)}, \quad (11)$$

in which γ is the phonon frequency at the Debye temperature (about 10^{13} s^{-1}), $N(E_F)$ is the density of localized states at the Fermi level, α is the inverse localization length of the wave function for the localized state, and λ is a dimensionless constant of about 18 [57]. Using Equation 10 and 11 for the temperature range of 120 K to 207 K at known σ_0 and T_0 (based on fitting the results shown in Fig. 6b with Equation 9), we determined that $N(E_F)$ and α were 2.61 x 10^{16} eV^{-1} cm^{-3} and 7.12 x 10^5 cm^{-1}, respectively. The other two Mott parameters, namely the average hopping distance (R) and the hopping energy (W), can also be evaluated by [64,65]

$$R = \left(\frac{9}{8\pi\alpha K_B T N(E_F)}\right)^{1/4} \quad (12)$$

and

$$W = \frac{3}{4\pi R^3 N\left(E_F\right)}. \tag{13}$$

Generally, W is the energy required for the inelastic tunneling transfer of a charge carrier between two localized states with the assistance of phonons. In VRH conduction, as proposed by Mott [65], the value of W should be on the order of a few K_BT while αR should be approximately unity. In our study, according to the calculated values of the Mott parameters for the temperature range of 120 K to 207 K (Table 1), R decreased with temperature, while W increased. The values of αR were also on the order of unity, demonstrating close agreement with the 3D mode of the VRH model. Understanding this carrier transport mechanism provides insight for improving perovskite-based devices for future applications.

4. Conclusions

In summary, we have investigated the metal contact and carrier transport behavior of perovskite by employing device patterning fabrication, and the TLM on the cm-sized single crystalline $CH_3NH_3PbBr_3$. The current injection at the contact interface follows thermionic emission theory, and we deduced the experimental Schottky barriers as 0.17 eV, 0.38 eV, and 0.47 eV for the Au, Pt, and Ti electrode contacts, respectively. We attributed the difference in the Schottky barriers of the three metals to their different work functions, imaging forces, and

interface pinning effects. We also discussed the image force-induced barrier height lowering effect and found that the height of the Schottky barriers in the absence of the image force were 0.22 eV (Au), 0.55 eV (Pt), and 0.74 eV (Ti). The Fermi level pinning effect was also observed near the interface, owing to electrons trapped by the surface states, which leads to charge rearrangement near the interface of the metal electrode and the $CH_3NH_3PbBr_3$. The temperature dependence of the sample's conductivity shows that the single crystal perovskite falls in an interface state induced thermally activated transport for the temperatures between 207 K to 300 K, though we observed 3D VRH conduction in the low temperature region of 120 K to 207 K. We also calculated and discussed the Mott parameters of the perovskite for the 3D VRH carrier transport model. Understanding these carriers transport mechanism helps us to predict the performance of perovskite devices when they operate at different temperatures. The study on the metal/perovskite Schottky contact and our analysis of carrier transport behavior in single crystal $CH_3NH_3PbBr_3$ establish a platform for developing further fundamental knowledge and practical applications of perovskite-based electronics and optoelectronic devices.

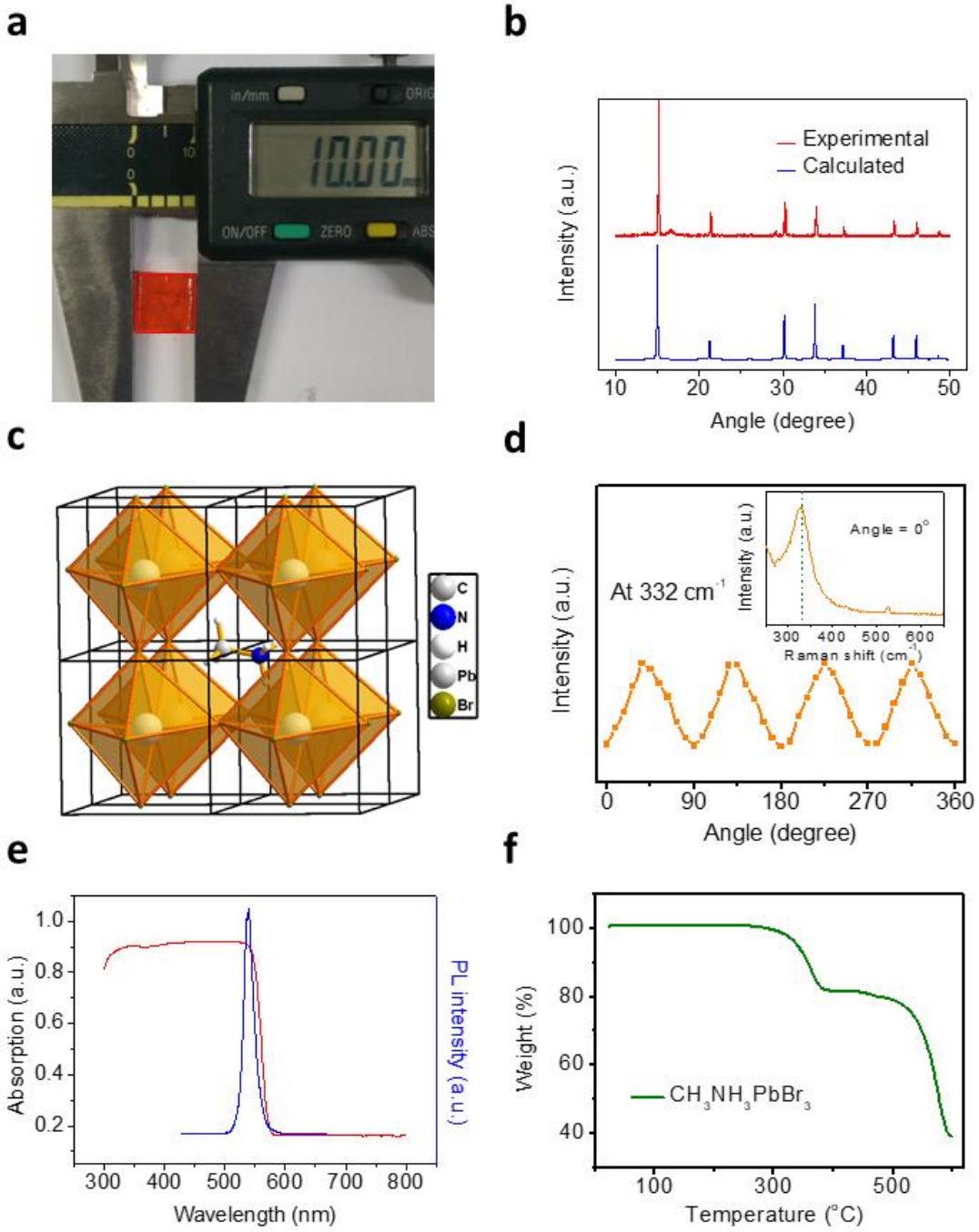

Fig. 1. Characterization of single crystal $CH_3NH_3PbBr_3$. (a) Photographic image of a single cubic $CH_3NH_3PbBr_3$ crystal. The length of one side is 10 mm. (b) The experimental and calculated XRD patterns demonstrate the high purity of the $CH_3NH_3PbBr_3$ perovskite. Single-crystal XRD

results are presented in the Supporting material. (c) Atomic model of $CH_3NH_3PbBr_3$ with cubic crystal structure. The $CH_3NH_3^+$ groups are at the corners, Br^- at the faces, and Pb^{2+} at the center of the cube. (d) The rotational angular dependence of the perovskite's Raman intensity at 332 cm^{-1}. The inset shows the Raman spectrum at 0º. (e) The photoluminescence (473 nm laser excitation) and optical absorption spectra of $CH_3NH_3PbBr_3$. (f) Thermogravimetric analysis of single crystal $CH_3NH_3PbBr_3$.

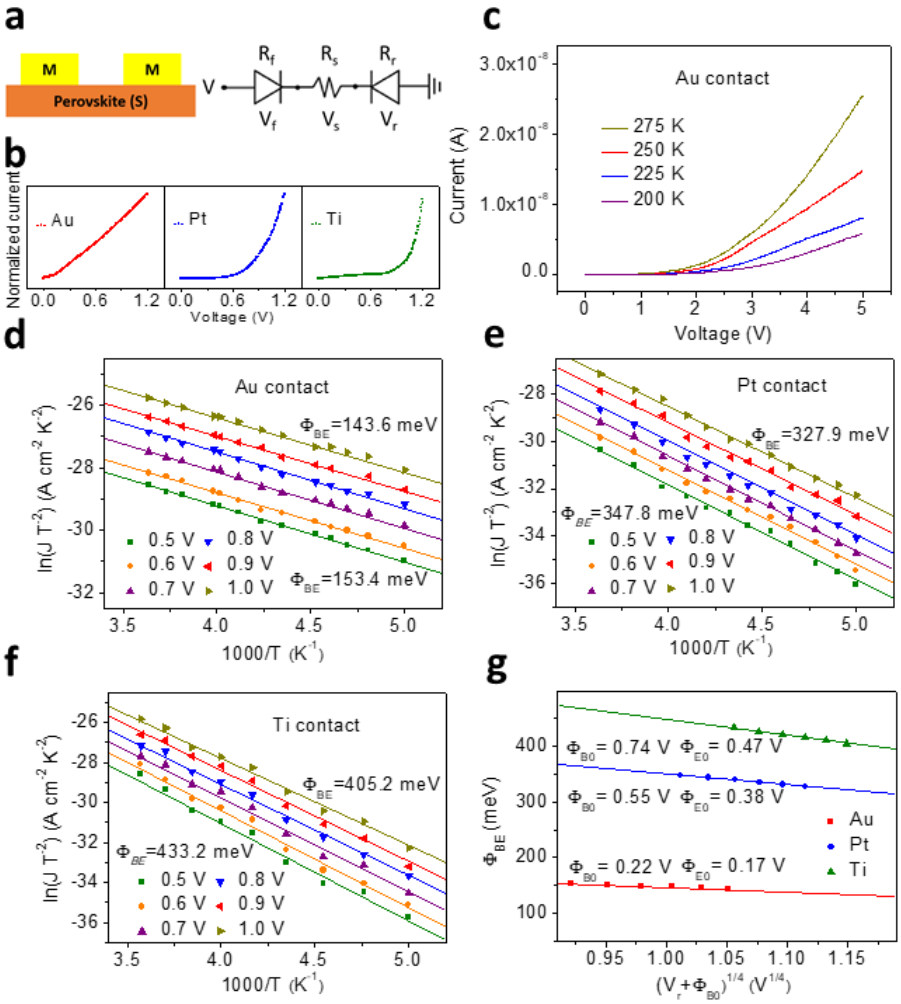

Fig. 2. *I-V* characteristics and Schottky barrier height analysis of the $CH_3NH_3PbBr_3$ perovskite contacted with Au, Pt, and Ti electrodes. (a) Equivalent circuit of the single crystal $CH_3NH_3PbBr_3$ contacted with metal. (b) Normalized current as a function of the applied voltage for the perovskite with Au, Pt, and Ti electrodes. The turn-on voltages are 0.22 V, 0.39 V, and 0.45 V for Au, Pt, and Ti contacts, defined by $I_{Vt}/I_{0.1} = e$, where I_{Vt} is the current at the turn-on voltage, $I_{0.1}$ is the current at 0.1 V, and e = 2.71828. (c) Two-probe current measurement of the perovskite with Au electrodes as a function of the applied voltage at different

temperatures. (d-f) Plots of $\ln(J\ T^{-2})$ vs. $1/T$ at several bias values from 0.5 V to 1 V for the perovskite featuring (d) the Au, (e) Pt, and (f) Ti contacts. (g) The plot of Φ_{BE} against $(V+\Phi_{B0})^{1/4}$ displays a linear relation, which shows the image force affects the Schottky barrier height significantly.

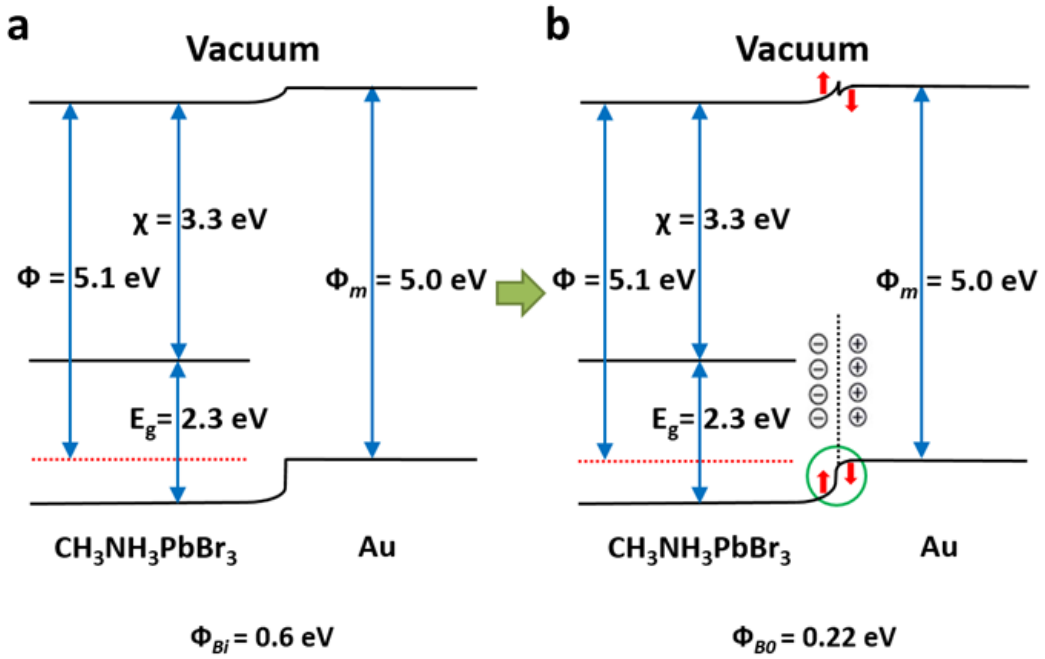

Fig. 3. A comparison of the band diagrams for the ideal Schottky barrier height and the Schottky barrier height in the absence of the image force for the Au/perovskite junction interface. The band diagrams of (a) display the ideal barrier height (Φ_{Bi}) and (b) the barrier height in the absence of the image force (Φ_{B0}) for the Au electrode in contact with the single crystal $CH_3NH_3PbBr_3$, demonstrating the pinning effect at the Schottky interface.

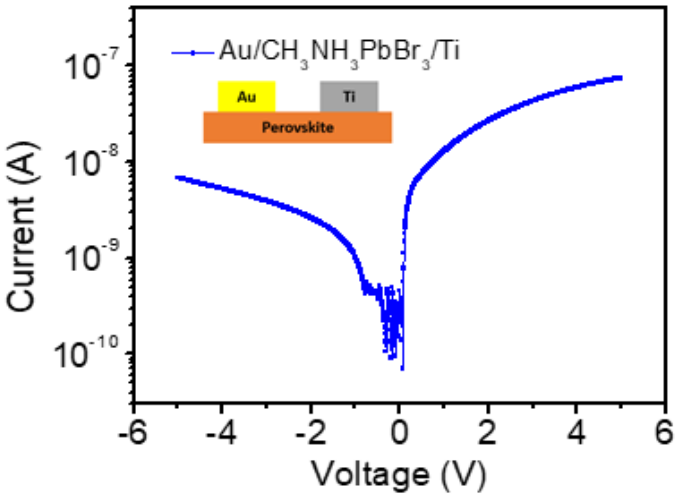

Fig. 4. *I-V* characteristics of Au/perovskite/Ti Schottky diode. The channel length between Au and Ti electrodes is around 100 μm.

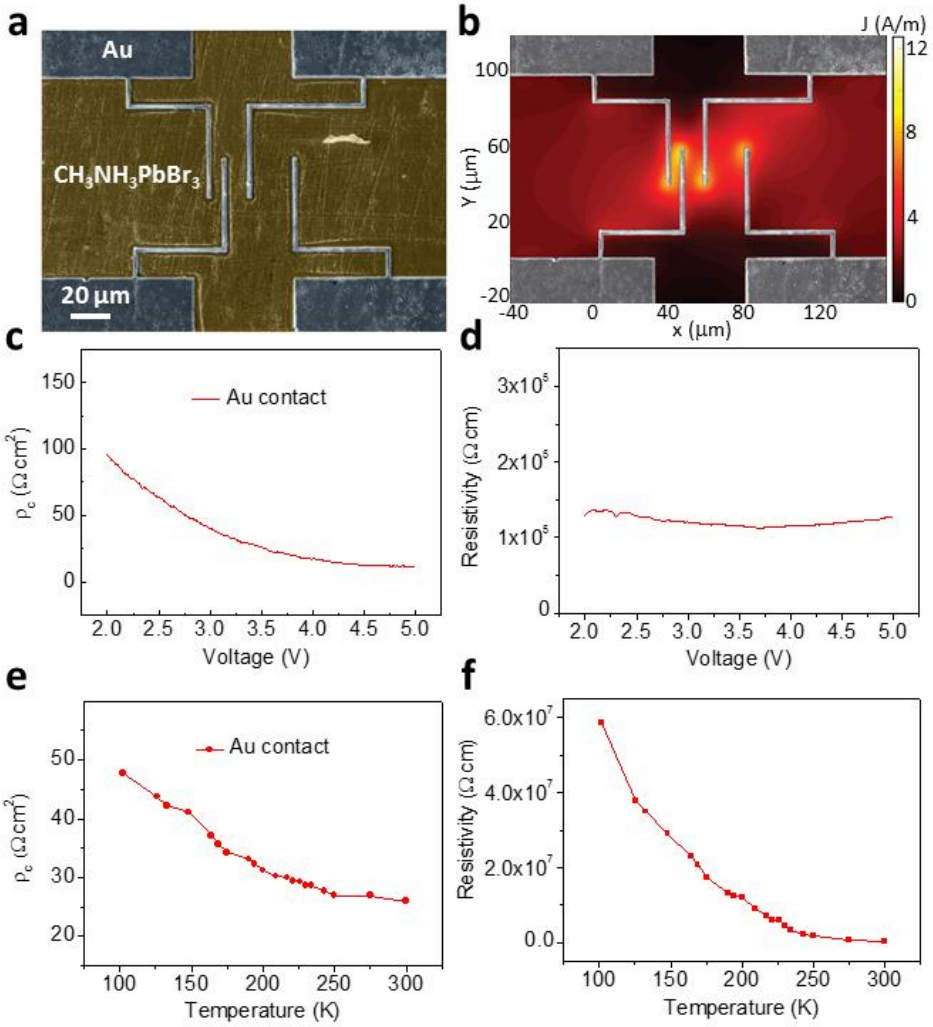

Fig. 5. The contact resistance and resistivity of $CH_3NH_3PbBr_3$ with a Au electrode, investigated using the TLM. (a) SEM image of the $CH_3NH_3PbBr_3$ perovskite featuring the TLM structure and (b) the simulated current flows of that structure. (c) The Au contact resistance (ρ_c) as a function of the applied voltage at 300 K. (d) The resistivity of $CH_3NH_3PbBr_3$ as a function of the applied voltage at 300 K. (e) The ρ_c of Au and (f) the bulk resistivity of the perovskite as a function of temperature from 100 K to 300 K at a bias of 3.5 V.

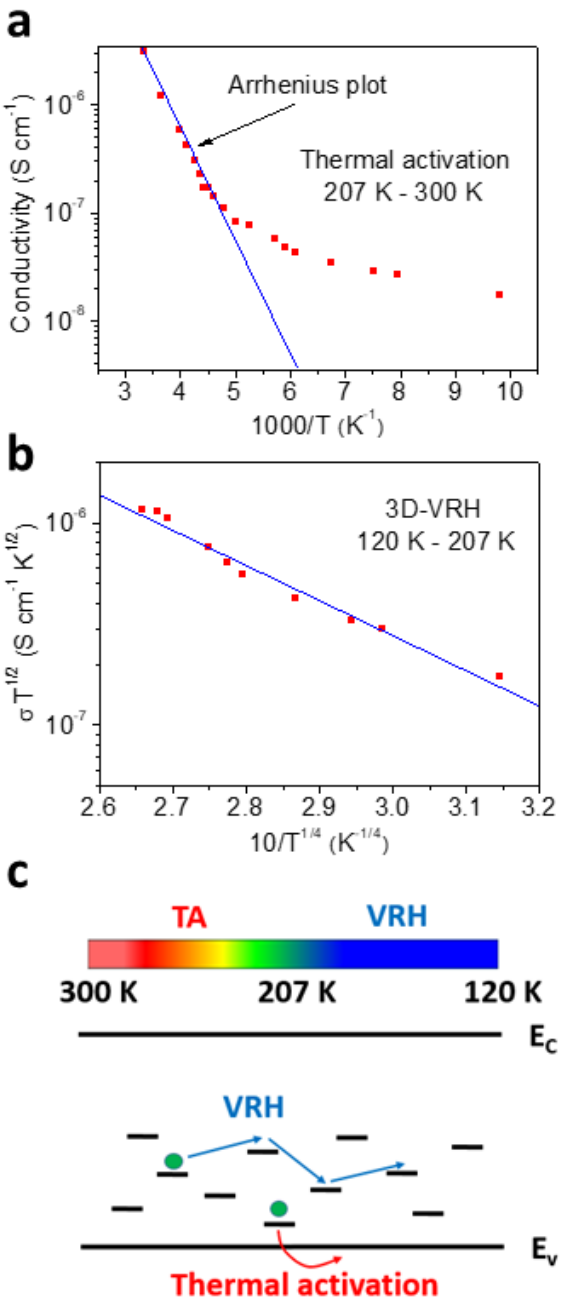

Fig. 6. The investigation of carrier transport mechanism near $CH_3NH_3PbBr_3$ perovskite surface using temperature-dependent conductivity. (a) Conductivity versus T^{-1} in log scale for the $CH_3NH_3PbBr_3$ perovskite. The linear relation in the temperature range from 207 K to 300 K suggests the material features thermally activated transport in this region. (b) A plot of $\sigma T^{1/2}$

versus $T^{-1/4}$ of $CH_3NH_3PbBr_3$ in log scale, demonstrating that VRH occurs in the temperature range of 120 K to 207 K. (c) A schematic diagram to show the mechanism of thermally activated transport and VRH conduction.

Table 1. Mott parameters for 3D VRH transport in the $CH_3NH_3PbBr_3$ perovskite.

T (K)	R (cm)	W (meV)	αR
207	5.73×10^{-6}	48.5	4.08
200	5.78×10^{-6}	47.3	4.11
175	5.98×10^{-6}	42.8	4.25
150	6.21×10^{-6}	38.1	4.42
125	6.50×10^{-6}	33.2	4.63

Acknowledgments

This work was financially supported by the King Abdullah University of Science and Technology (KAUST) Office of Sponsored Research (OSR) (OSR-2016-CRG5-3005), KAUST solar center (FCC/1/3079-08-01), and KAUST baseline funding.

Competing Interests

The authors declare no competing financial or non-financial interests.

Appendix A. Supplementary material

Supplementary data associated with this article can be found in the online version at http://dx.doi.org.

References

[1] J. Kim, S. H. Lee, J. H. Lee, K. H. Hong, J. Phys. Chem. Lett. 5 (2014) 1312–1317.

[2] S. D. Stranks, H. J. Snaith, Nature Nanotech. 10 (2015) 391–402.

[3] M. M. Lee, J. Teuscher, T. Miyasaka, T. N. Murakami, H. J. Snaith, Science 338 (2012) 643–647.

[4] H. S. Kim, C. R. Lee, J. H. Im, K. B. Lee, T. Moehl, A. Marchioro, S. J. Moon, R. H. Baker, J. H. Yum, J. E. Moser, M. Grätzel, N. G. Park, Sci. Rep. 2 (2012) 591.

[5] N. J. Jeon, J. H. Noh, W. S. Yang, Y. C. Kim, S. Ryu, J. Seo, S. I. Seok, Nature 517 (2015) 476–480.

[6] N. G. Park, J. Phys. Chem. Lett. 4 (2013) 2423–2429.

[7] Z. K. Tan, R. S. Moghaddam, M. L. Lai, P. Docampo, R. Higler, F. Deschler, M. Price, A.

Sadhanala, L. M. Pazos, D. Credgington, F. Hanusch, T. Bein, H. J. Snaith, R. H. Friend, Nature Nanotech. 9 (2014) 687–692.

[8] T. Kondo, T. Azuma, T. Yuasa, R. Ito, Solid State Commun. 105 (1998) 253–255.

[9] J. Song, J. Li, X. Li, L. Xu, Y. Dong, H. Zeng, Adv. Mater. 27 (2015) 7162–7167.

[10] J. Huang, Y. Shao, Q. Dong, J. Phys. Chem. Lett. 6 (2015) 3218–3227.

[11] W. Nie, H. Tsai, R. Asadpour, J. C. Blancon, A. J. Neukirch, G. Gupta, J. J. Crochet, M. Chhowalla, S. Tretiak, M. A. Alam, H. L. Wang, A. D. Mohite, Science 30 (2015) 522–525.

[12] M. D. McGehee, Nat. Mater. 13 (2014) 845–846.

[13] N. Hannay, Electronic Materials, Plenum Press, New York, 1973.

[14] Y. Dang, Y. Liu, Y. Sun, D. Yuan, X. Liu, W. Lu, G. Liu, H. Xia, X. Tao, CrystEngComm 17 (2015) 665–670.

[15] Q. Dong, Y. Fang, Y. Shao, P. Mulligan, J. Qiu, L. Cao, J. Huang, Science 347 (2015) 967–970.

[16] D. Shi, V. Adinolfi, R. Comin, M. Yuan, E. Alarousu, A. Buin, Y. Chen, S. Hoogland, A. Rothenberger, K. Katsiev, Y. Losovyj, X. Zhang, P. A. Dowben, O. F. Mohammed, E. H. Sargent, O. M. Bakr, Science 347 (2015) 519–522.

[17] M. I. Saidaminov, A. L. Abdelhady, B. Murali, E. Alarousu, V. M. Burlakov, W. Peng, I.

Dursun, L. Wang, Y. He, G. Maculan, A. Goriely, T. Wu, O. F. Mohammed, O. M. Bakr, Nature Commun. 6 (2015) 7586.

[18] Y. Fang, Q. Dong, Y. Shao, Y. Yuan, J. Huang, Nature Photonics 9 (2015) 679–686.

[19] H. H. Fang, S. Adjokatse, H. Wei, J. Yang, G. R. Blake, J. Huang, J. Even, M. A. Loi, Sci. Adv. 2 (2016) e1600534.

[20] W. Peng, L. Wang, B. Murali, K. T. Ho, A. Bera, N. Cho, C. F. Kang, V. M. Burlakov, J. Pan, L. Sinatra, C. Ma, W. Xu, D. Shi, E. Alarousu, A. Goriely, J. H. He, O. F. Mohammed, T. Wu, O. M. Bakr, Adv. Mater. 28 (2016) 3383–3390.

[21] S. M. Sze, K. K. Ng, Physics of Semiconductor Devices, John Wiley & Sons, New Jersey, 2007.

[22] G. Niu, X. Guo, L. Wang, J. Mater. Chem. A 3 (2015) 8970–8980.

[23] L. A. Majewski, J. W. Kingsley, C. Balocco, A. M. Song, Appl. Phys. Lett. 88 (2006) 222108.

[24] Sigma-Aldrich: Analytical, Biology, Chemistry & Materials Science Products and Services, http://www.sigmaaldrich.com/ (accessed Jul, 2018).

[25] Gold Price, http://goldprice.org/ (accessed Jul, 2017).

[26] D. Li, H. Wu, H. C. Cheng, G. Wang, Y. Huang, X. Duan, ACS Nano 10 (2016) 6933–6941.

[27] M. Karakus, S. A. Jensen, F. D'Angelo, D. Turchinovich, M. Bonn, E. Cánovas, J. Phys. Chem. Lett. 6 (2015) 4991–4996.

[28] S. P. Senanayak, B. Yang1, T. H. Thomas, N. Giesbrecht, W. Huang, E. Gann, B. Nair, K. Goedel, S. Guha, X. Moya, C. R. McNeill, P. Docampo, A. Sadhanala, R. H. Friend, H. Sirringhaus, Science Advances 3 (2017) e1601935.

[29] C. S. Ponseca Jr., T. J. Savenije, M. Abdellah, K. Zheng, A. Yartsev, T. Pascher, T. Harlang, P. Chabera, T. Pullerits, A. Stepanov, J. P. Wolf, V. Sundström, J. Am. Chem. Soc. 136 (2014) 5189–5192.

[30] X. Y. Chin, D. Cortecchia, J. Yin, A. Bruno, C. Soci, Nature Commun. 6 (2015) 7383.

[31] A. Venugopal, L. Colombo, E. M. Vogel, Appl. Phys. Lett. 96 (2010) 013512.

[32] F. Xia, V. Perebeinos, Y. M. Lin, Y. Wu, P. Avouris, Nature Nanotech. 6 (2011) 179–184.

[33] L. Wang, I. Meric, P. Y. Huang, Q. Gao, Y. Gao, H. Tran, T. Taniguchi, K. Watanabe, L. M. Campos, D. A. Muller, J. Guo, P. Kim, J. Hone, K. L. Shepard, C. R. Dean, Science 342 (2013) 614–617.

[34] Y. Xu, C. Cheng, S. Du, J. Yang, B. Yu, J. Luo, W. Yin, E. Li, S. Dong, P. Ye, X. Duan, ACS Nano 10 (2016) 4895–4919.

[35] K. T. Butler, J. M. Frost, A. Walsh, Mater. Horiz. 2 (2015) 228–231.

[36] V. Sorianello, L. Colace, M. Nardone, G. Assanto, Thin Solid Films 519 (2011) 8037–

8040.

[37] T. C. Wei, S. Mokkapati, T. Y. Li, C. H. Lin, G. R. Lin, C. Jagadish, J. H. He, Adv. Funct. Mater. 28 (2018) 1707175.

[38] H. Zhou, Q. Chen, G. Li, S. Luo, T. b. Song, H. S. Duan, Z. Hong, J. You, Y. Liu, Y. Yang, Science 345 (2014) 542–546.

[39] E. Edri, S. Kirmayer, M. Kulbak, G. Hodes, D. Cahen, J. Phys. Chem. Lett. 5 (2014) 429–433.

[40] S. Aharon, B. E. Cohen, L. Etgar, J. Phys. Chem. C 118 (2014) 17160–17165.

[41] Y. Shimura, K. Nomura, H. Yanagi, T. Kamiya, M. Hirano, H. Hosono, Thin Solid Films 516 (2008) 5899–5902.

[42] J. J. Ke, K. T. Tsai, Y. A. Dai, J. H. He, Appl. Phys. Lett. 100 (2012) 053503.

[43] E. H. Rhoderick, Metal-Semiconductor Contacts, Clarendon Press, Oxford, 1980.

[44] Z. Y. Zhang, K. Yao, Y. Liu, C. H. Jin, X. L. Liang, Q. Chen, L. M. Peng, Adv. Funct. Mater. 17 (2007) 2478–2489.

[45] Z. Y. Zhang, C. H. Jin, X. L. Liang, Q. Chen, L. M. Peng, Appl. Phys. Lett. 88 (2006) 073102.

[46] E. H. Rhoderick, J. Phys. D Appl. Phys. 5 (1972) 1920–1929.

[47] L. Xia, W. Wu, Y. Hao, Y. Wang, Appl. Phys. Lett. 88 (2006) 152108.

[48] C. Y. Nam, D. Tham, J. E. Fischer, Nano Lett. 5 (2005) 2029–2033.

[49] B. Murali, S. Dey, A. L. Abdelhady, W. Peng, E. Alarousu, A. R. Kirmani, N. Cho, S. P. Sarmah, M. R. Parida, M. I. Saidaminov, A. A. Zhumekenov, J. Sun, M. S. Alias, E. Yengel, B. S. Ooi, A. Amassian, O. M. Bakr, O. F. Mohammed, ACS Energy Lett. 1 (2016) 1119–1126.

[50] G. Yang, H. Tao, P. Qin, W. Ke, G. Fang, J. Mater. Chem. A 4 (2016) 3970–3990.

[51] Z. H. Bakr, Q. Wali, A. Fakharuddin, L. Schmidt-Mende, T. M. Brown, R. Jose, Nano Energy 34 (2017) 271–305.

[52] D. Li, H. C. Cheng, H. Wu, Y. Wang, J. Guo, G. Wang, Y. Huang, X. Duan, J. Phys. Chem. Lett. 8 (2017) 429–434.

[53] D. K. Schroder, Semiconductor Material and Device Characterization, John Wiley & Sons, New York, 2006.

[54] C. Y. Ho, S. H. Chiu, J. J. Ke, K. T. Tsai, Y. A. Dai, J. H. Hsu, M. L. Chang, J. H. He, Nanotechnology 21 (2010) 134008.

[55] E. Stern, G. Cheng, M. P. Young, M. A. Reed, Appl. Phys. Lett. 88 (2006) 053106.

[56] Y. Takahashi, R. Obara, K. Nakagawa, M. Nakano, J. y. Tokita, T. Inabe, Chem. Mater. 19 (2007) 6312–6316.

[57] Y. Natsume, H. Sakata, T. Hirayama, Status Solidi A 148 (1995) 485–495.

[58] C. Eames, J. M. Frost, P. R. F. Barnes, B. C. O'Regan, A. Walsh, M. S. Islam, Nature Commun. 6 (2015) 7497.

[59] Y. Zhao, C. Liang, H. Zhang, D. Li, D. Tian, G. Li, X. Jing, W. Zhang, W. Xiao, Q. Liu, F. Zhang, Z. He, Energy Environ. Sci. 8 (2015) 1256–1260.

[60] R. L. Milot, G. E. Eperon, H. J. Snaith, M. B. Johnston, L. M. Herz, Adv. Funct. Mater. 25 (2015) 6218–6227.

[61] T. J. Savenije, C. S. Ponseca Jr., L. Kunneman, M. Abdellah, K. Zheng, Y. Tian, Q. Zhu, S. E. Canton, I. G. Scheblykin, T. Pullerits, A. Yartsev, V. Sundström, J. Phys. Chem. Lett. 5 (2014) 2189–2194.

[62] D. Li, G. Wang, H. C. Cheng, C. Y. Chen, H. Wu, Y. Liu, Y. Huang, X. Duan, Nat. Commun. 7 (2016) 11330.

[63] P. S. Whitfield, N. Herron, W. E. Guise, K. Page, Y. Q. Cheng, I. Milas, M. K. Crawford, Sci. Rep. 6 (2016) 35685.

[64] Z. H. Khan, M. Husain, T. P. Perng, N. Salah, S. Habib, J. Phys. Condens. Matter 20 (2008) 475207.

[65] N. F. Mott, E. A. Davis, Electronic Processes in Non-Crystalline Materials, Clarendon Press, Oxford, 2012.

Chun-Ho Lin:

Mr. Chun-Ho Lin is a PhD student at Computer, Electrical and Mathematical Sciences and Engineering (CEMSE) Division, King Abdullah University of Science & Technology (KAUST). He received the B.S. degree in physics and M.S. degree in electrical engineering from National Taiwan University in 2011 and 2014, respectively. He puts his efforts in the development of flexible electronics using novel devices based on nanomaterials. He is also currently involving in fundamental physical properties hybrid perovskite and their optoelectronics applications.

Ting-You Li

Mr. Ting-You Li is a PhD student at Computer, Electrical and Mathematical Sciences and Engineering (CEMSE) Division, King Abdullah University of Science & Technology (KAUST). He has received his M.S. degree in electrical engineering from KAUST in 2017. He puts his efforts in the development of perovskite single crystal growing and perovskite-based devices.

Bin Cheng

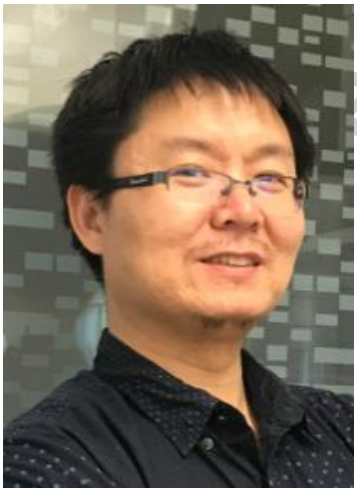

Dr. Bin Cheng received his PhD degree (2015) from Department of Physics in University of California, Riverside. Currently, he is a Post-Doctoral Fellow at Electrical Engineering Department at King Abdullah University of Science and Technology (KAUST). His research interests focus on transport and optoelectronic properties on two-dimensional materials such as graphene, TMDs and layered hybrid perovskites.

Changxu Liu

Changxu got his BS with highest honor from Department of Electronic Science and Technology, Tongji University, Shanghai, China in 2008. Then he received his MS in EE from University of Rochester, NY, USA in 2010. In 2011, he joined KAUST as a PhD student in PRIMALIGHT, under the supervision of Prof. Andrea Fratalocchi. His research mainly focused on the light-matter interaction in complex systems. Together with his advisor, they have published several papers in highly visible journals such as Nature Nanotechnology, Nature Photonics, Nature Physics, Physical Review X and Nano Letters.

Chih-Wen Yang

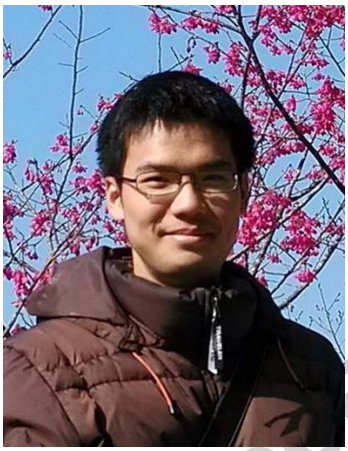

Mr. Chih-Wen Yang is a PhD student at Physical Science and Engineering Division (PSE) Division, King Abdullah University of Science & Technology (KAUST). He has received his M.S. degree in material science from National Tsing Hua University in Taiwan. He puts his efforts in the development of 2D materials growing and inorganic nanomaterials-based devices.

Jr-Jian Ke

Jr-Jian Ke received the B.S. degree in electrical engineering from National University of Kaohsiung, Taiwan, in 2007. He received his M.S. and Ph.D. degree from Graduate Institute of Photonics and Optoelectronics at the National Taiwan University, Taiwan, in 2009 and 2016, respectively. His past research actives include the resistive memory, surface effects in nanostructures and electron conduction mechanisms.

Tzu-Chiao Wei

Tzu-Chiao Wei received the B.Sc. degree from Fu Jen Catholic University in 2008, and the M.Sc. degree from National Central University in 2010. His master's thesis was titled "The research of filter for direction-limited light source" supervised by Professor Cheng-Chung Lee. He received the Ph.D. degrees from the National Taiwan University in 2017. Dissertation was titled "Optical properties of perovskite" supervised by Professor Gong-Ru Lin and Professor Jr-Hau He. He engages in multidisciplinary fields including optical interference filter fabrication, optical analysis of semiconductor, theoretical and experimental research on photodetector, nonlinear optics absorption applications, Raman spectroscopy, strain measurement, nano-structured composite and colorimetry.

Lain-Jong Li

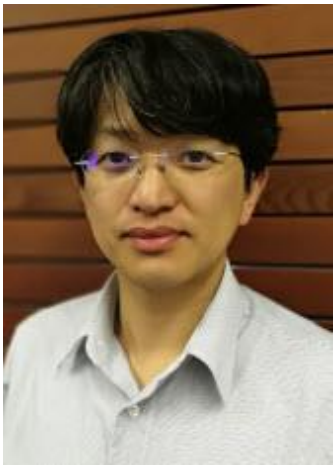

Lain-Jong (Lance) Li is an associate Professor at KAUST. He received his PhD from condensed matter physics at Oxford University in 2006. His current research interest focuses on the growth and characterizations of 2-dimensional materials including graphene and transition metal dichalcogenides. He has obtained Humboldt Research Fellowship for Experienced Researchers (Germany) and Career Development Award Taiwan. He has authored more than 160 contributions in international journals, 30 invited talks and more than 40 patents.

Andrea Fratalocchi

Dr. Andrea Fratalocchi is an Assistant Professor in the Computer, Electrical and Mathematical Sciences and Engineering Division. His research interests focus in the use of disorder as a building block for a new technology, which can benefit from the billenary evolution of natural systems. His vision is to grab the hidden secrets of randomness to unveil novel fundamental processes and a new class of electromagnetic materials that can be assembled on large sizes with minimal costs.

Jr-Hau He:

Dr. Jr-Hau He is an Associate Professor of Electrical Engineering program at King Abdullah University of Science & Technology (KAUST). He has been a pioneer in optoelectronics, which reflects on his achievement of photon management on the light harvesting devices. He has conducted highly interdisciplinary researches to bridge those gaps between various research fields and between academia and industry. He is a Fellow of RSC and SPIE, and a senior member of IEEE and OSA.

Highlights

- The Schottky barrier height study of $CH_3NH_3PbBr_3$ single crystals with Pt, Au, and Ti contacts.
- The carrier transport study in the temperature ranging from 100 K to 300 K near $CH_3NH_3PbBr_3$ perovskite surface.